Annu. Rev. Mater. Res. 2002. 32:377–400
doi: 10.1146/annurev.matsci.32.111201.142017

ATOMISTIC ASPECTS OF CRACK PROPAGATION IN BRITTLE MATERIALS: Multimillion Atom Molecular Dynamics Simulations

Cindy L. Rountree, Rajiv K. Kalia, Elefterios Lidorikis,[1] Aiichiro Nakano, Laurent Van Brutzel,[2] and Priya Vashishta
Concurrent Computing Laboratory for Materials Simulations, Department of Physics and Astronomy and Department of Computer Science, Louisiana State University, Baton Rouge, Louisiana 70803-4001; e-mails: rountree@rouge.phys.lsu.edu; kalia@bit.csc.lsu.edu; nakano@bit.csc.lsu.edu; priyav@bit.csc.lsu.edu

Key Words fracture, multiscale, roughness exponent, ceramics

■ **Abstract** Atomistic aspects of dynamic fracture in a variety of brittle crystalline, amorphous, nanophase, and nanocomposite materials are reviewed. Molecular dynamics (MD) simulations, ranging from a million to 1.5 billion atoms, are performed on massively parallel computers using highly efficient multiresolution algorithms. These simulations shed new light on (*a*) branching, deflection, and arrest of cracks; (*b*) growth of nanoscale pores ahead of the crack and how pores coalesce with the crack to cause fracture; and (*c*) the influence of these mechanisms on the morphology of fracture surfaces. Recent advances in novel multiscale simulation schemes combining quantum mechanical, molecular dynamics, and finite-element approaches and the use of these hybrid approaches in the study of crack propagation are also discussed.

INTRODUCTION

Basic Concepts of Fracture

The study of fracture spans many disciplines in the physical sciences and engineering. Over the past century, a number of developments have occurred that significantly advance our understanding of fracture at the macroscopic scale. One of the earliest and most important developments in this field was a criterion developed by Griffith for the extension of an isolated crack in a solid under the influence of an applied stress (1, 2, 3). Griffith based his criterion on simple

[1]Current address: Department of Physics, Massachusetts Institute of Technology, Cambridge, Massachusetts 02139; e-mail: lidorki@phys.mit.edu
[2]Current address: CEA-Centre de Valrhô, LCLT site de Marcóule-BP17171, 30207 Bagnol Surceze cedex, France; e-mail: laurent.vanbrutzel@cea.fr

energetic and thermodynamic considerations and on an earlier work of Inglis for stresses around an elliptical cavity in a plate under uniform tension (4). Inglis had found that local stresses around sharp corners were much higher than the applied tension. Realizing that flaws in a solid would act as stress concentrators, Griffith applied Inglis' analysis to a static crack of length c in an elastic body under a uniform stress at its outer boundaries. Partitioning the energy of the system U into a surface contribution for creating new surfaces and using a mechanical contribution from the applied stress and the potential energy of the elastic solid,

$$U(c) = -\frac{\pi c^2 \sigma^2}{E'} + 4c\gamma, \qquad 1.$$

Griffith showed that failure occurs when the applied stress, σ, exceeds a critical value,

$$\sigma_c = \left(\frac{2E'\gamma}{\pi c_0}\right)^{1/2}, \qquad 2.$$

for a crack of length c_0. In the above Equations, γ is the surface energy and E' is either the Young's modulus E (in plane stress) or $E/(1-\nu^2)$ (in plane strain, ν is the Poisson ratio). The critical stress, σ_c, is not an intrinsic material characteristic as it depends on the crack length.

The energy-balance concept and the thermodynamic view of crack extension in a continuum solid became the foundation of a vast analytical field known as fracture mechanics, whose rapid development was spurred by the need to have reliable safety criteria for engineering design. Around 1950, Irwin and co-workers put Griffith's concepts into a broader context by introducing a quantity called the mechanical-energy-release rate, G, which is the change in the mechanical energy per unit area of the crack surface caused by an incremental increase in the crack length (5). It should be noted that G is independent of how the external loads are applied.

Another important concept in fracture mechanics arose in the context of stress distribution around the crack tip. For an isotropic linear material it was shown (6–9) that the stress near the crack tip varies as (see Figure 1):

$$\sigma_{ij}^{(a)}(r,\theta) = \frac{K_{(a)}}{\sqrt{2\pi r}} f_{ij}^{(a)}(\theta), \qquad 3.$$

where the index a represents the mode of fracture (see Figure 2) and f_{ij} is a dimensionless function of the angle θ and the fracture mode. The quantity K is a measure of the intensity of the stress field near the crack tip and is therefore known as the stress intensity factor. K also depends on the mode of fracture, the geometry of the crack, and material characteristics. At the onset of crack propagation, the value of K depends only on material characteristics, and this critical value, K_c, is known as the fracture toughness. It is a measure of a material's resistance to crack

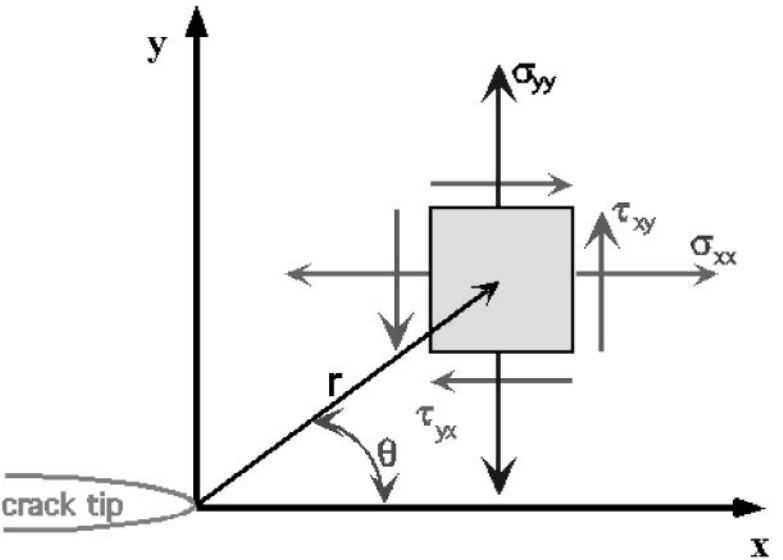

Figure 1 Schematic in two dimensions showing various stress components around the crack tip. σ_{xx} and σ_{yy} are the normal components, and τ_{xy} and τ_{yx} are the shear components of the stress.

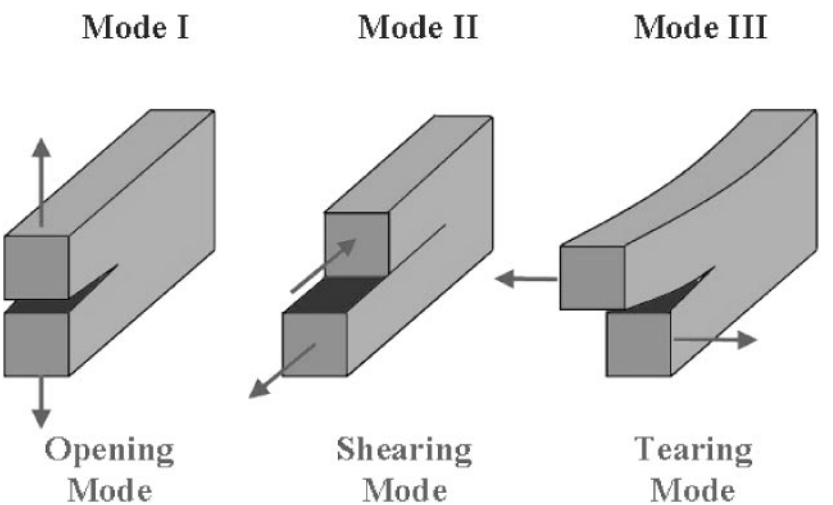

Figure 2 Three modes of fracture in a cracked body: Mode I is the opening mode, mode II is the shearing mode in the crack plane, and mode III is the tearing mode.

propagation. A unique relationship exists between K_c and the critical value of the mechanical-energy-release rate:

$$K_c = (G_c E')^{1/2}. \quad 4.$$

Importance of Atomistic Aspects of Fracture

A serious shortcoming of fracture mechanics is the spurious singularity of the stress field at the crack tip (Equation 3). Theoretically, this problem can only be addressed by investigating various processes occurring near the crack tip during crack propagation (10, 11). A proper theoretical description of fracture must include not only nonlinearities in the vicinity of the crack but also bond breaking between atoms, as well as the formation of extended defects (e.g., dislocations). Thus what is required near the crack tip is a departure from continuum mechanics and an atomic description of fracture. Molecular dynamics (MD) has become the method of choice to study fracture at the atomic scale. MD simulations provide the dynamics of atoms through Newton's equations of motion. The equations are discretized in time and then integrated with a finite-difference algorithm to obtain atomic trajectories (positions and velocities of atoms as functions of time). The trajectories allow the determination of structural, dynamical, thermal, and mechanical properties of the system. The MD approach includes nonlinearities in the system, and it can easily provide atomic-level stresses and strains as well as the dynamics of cracks.

Earlier attempts to model fracture at the atomistic level were based on network spring or lattice static models (12–14). In recent years, MD simulations have been performed with reliable interatomic interactions for various metals, ceramics, and composites (for more detail, see below). The interactions have been validated through detailed comparison with experimental measurements and first-principles quantum-mechanical calculations.

Another recent development with significant impact on research on atomistic aspects of fracture is the emergence of parallel computers and highly efficient algorithms. In the past few years, massively parallel computers delivering teraflop (10^{12} floating point operations per second) performance have become available. When combined with highly efficient, linearly scaling algorithms for MD simulations, parallel architectures have made it possible to simulate $\sim 10^9$ atom systems with realistic interactions. Furthermore, data compression algorithms and advanced visualization tools for three-dimensional, immersive, and interactive visualization environments have greatly helped to obtain new information from massively parallel MD simulations.

Multiple Length Scale Simulations

Two significant developments have recently occurred to further enhance the reliability of atomistic simulations. To adequately handle chemical processes involving bond breakage and formation, schemes have been developed to couple MD

with a suitable quantum-mechanical description. (To some extent, charge-transfer schemes for ionic-covalent materials and bond-order potentials for purely covalent systems attempt to include chemical processes in a MD simulation.)

One of the most appropriate quantum-mechanical approaches is based on the density functional theory (DFT). In DFT, a Schrödinger-like equation (15), called the Kohn-Sham equation, is solved. The effective interaction in the Kohn-Sham equation is a sum of the electron-ion interaction, the Coulomb potential between electrons, and an exchange-correlation potential (16, 17). In 1985, Car & Parrinello introduced an innovative approach to couple the dynamics of nuclei with the solution of the Kohn-Sham equation for electrons (18). This approach provides an appropriate description of bond breakage around the crack tip during crack propagation. A computationally simpler approach than the DFT, the so-called tight-binding approach, has also been used to handle electronic processes near the crack tip (19–21). Currently, the DFT calculations are limited to several hundred atoms and those involving the tight-binding method to 10^4 atoms. Clearly, these approaches by themselves cannot handle large enough systems for the study of fracture.

To study fracture, quantum-mechanical (QM) approaches have been successfully merged with MD schemes based on empirical interatomic potentials whose parameters are derived from DFT calculation (22–25). In these coupled QM/MD simulations, the region close to the crack tip is taken to be a QM cluster embedded in a MD system. The total energy of the whole system is approximately equal to the energies computed with the MD approach and the difference between the energy of the cluster evaluated separately by QM and MD methods. The details of this scheme are discussed below. In addition to coupling QM methods with MD, considerable progress has been made in linking MD and continuum descriptions. In one of the hybrid MD/continuum schemes, the region surrounding the crack tip is described by MD or a combination of QM and MD schemes. Sufficiently far from the crack tip, the equations of linear elasticity are solved on a computational grid using the finite-element (FE) method. The FE nodes obey Hamiltonian dynamics with nodal accelerations calculated from the stiffness matrix and the lumped mass approximation (see below). At the interface of the MD and FE regions, a "handshake" scheme involving an average of the MD and FE Hamiltonians is implemented (26–29). Another viable MD/FE approach involves an atomic description coupled with a statistical coarse-grained procedure to remove certain degrees of freedom (30).

Tadmor et al. have developed a scheme, called the quasi-continuum method, to join atomistic and FE approaches (31). An interatomic potential is used to define an energy functional for the deformed system. The FE grid is adaptively refined in regions of high deformation such as slip planes or grain boundaries. The equilibrium is found via a zero temperature relaxation technique. This method has been successfully used to study interactions between grain boundaries, dislocations, cracks, and nanoindentation.

In this article, the basic concepts of molecular dynamics and algorithms for parallel implementation are first reviewed. Next a review of results for dynamic

fracture in graphite and crystalline GaAs, as well as in crystalline, amorphous, and nanophase Si_3N_4, SiO_2, and nanocomposite materials, is presented. Comparisons between simulation and experimental results for scaling properties of cracks and fracture surfaces are also presented in this section. Methodologies for coupling quantum mechanical, molecular dynamics, and finite-element approaches are then described and conclusions are given.

MOLECULAR DYNAMICS: ALGORITHMS AND PARALLEL IMPLEMENTATION

Molecular dynamics (MD) is the primary simulation approach used to investigate fracture at the atomic level. This method involves the solution of classical equations of motion for a system of N atoms. In classical statistical mechanics, the phase-space trajectories, $\{\vec{r}_i(t), \vec{v}_i(t)\}$, are calculated by integrating Newton's second law:

$$m_i \ddot{\vec{r}}_i = \vec{f}_i = -\frac{\partial \phi(\vec{r}_1, \vec{r}_2, \ldots, \vec{r}_N)}{\partial \vec{r}_i}, \qquad 5.$$

where $\phi(\vec{r}_1, \vec{r}_2, \ldots, \vec{r}_N)$ is the interatomic potential and $\vec{f}_i$ is the force on the i^{th} atom. To solve the set of $3N$ equations in Equation 5, the initial and boundary conditions need to be specified. In the case of a crystal, the initial conditions are the lattice positions; for an amorphous material, the initial configuration is obtained by quenching a molten state. The initial set of atomic velocities is chosen randomly from a Maxwell-Boltzmann distribution.

A number of robust algorithms are available to integrate the Equation 5 (32). All require finite differencing and a suitable time step, Δt, that conserves the total Hamiltonian of the system (typically, Δt is on the order of a femtosecond). Another important criterion in choosing an integration algorithm is that the time reversibility of Newton's equations of motion is preserved. An example of a time-reversible algorithm is the velocity-Verlet algorithm (33, 34).

Interactomic Potentials

The essential input to a MD simulation is the interatomic potential. The degree to which the results of MD simulation represent the properties of real materials is determined by how realistic the potential is. The functional complexity of an interatomic potential determines the amount of time needed for the simulation. Over the years a vast number of potentials have been developed that include pair potentials (35, 36), embedded-atom potentials (37, 38), bond-order potentials, etc. (39, 40). A brief survey of some of these potentials along with the different classes (ionic, covalent, and metallic) of materials they describe is given below.

For an N-atom system, the potential energy may be written as

$$\phi(\vec{r}_i, \ldots \vec{r}_N) = \sum_i^N \phi_1(\vec{r}_i) + \frac{1}{2!}\sum_{i,j}^N \phi_2(\vec{r}_i, \vec{r}_j) + \frac{1}{3!}\sum_{i,j,k}^N \phi_3(\vec{r}_i, \vec{r}_j, \vec{r}_k) + \cdots, \quad 6.$$

where the first term is a one-body potential, the second term is a pair-wise potential, and the last term is a three-body potential. A one-body potential may represent the effect of an external field. Examples of commonly used pair-wise potentials are the Lennard-Jones and Coulomb interactions. A widely used functional form for the three-body term is the Stillinger-Weber potential (41), which consists of interactions between triplets of atoms and represents the bond-stretching and bond-bending contributions in covalent materials.

We are primarily interested in ceramics, which are both ionic and covalent in character. For these materials it is necessary to combine two- and three-body interactions. The two-body potential as a function of the interatomic separation, r_{ij}, has the form:

$$\phi_{ij}(r_{ij}) = \frac{H_{ij}}{r_{ij}^{\eta_{ij}}} + \frac{Z_i Z_j}{r_{ij}} e^{-r_{ij}/r_{1s}} - \frac{1}{2}\frac{\left(\alpha_i Z_j^2 + \alpha_j Z_i^2\right)}{r_{ij}^4} e^{-r_{ij}/r_{4s}}, \quad 7.$$

where the first term represents steric repulsion, the second term is the Coulomb interaction owing to the charge transfer, and the last term corresponds to charge-dipole interaction. The parameters (H, η, Z, etc.) are determined by fitting to the experimental structure, phonon densities of states and mechanical properties (36, 42, 43).

The three-body interaction commonly used in ceramics and semiconductors has the same functional form as the Stillinger-Weber potential:

$$\phi_{jik}(r_{ij}, r_{ik}, \cos\theta_{jik}) = B_{jik}\, f_{ij}(r_{ij})\, f_{ik}(r_{ik})[\cos\theta_{jik} - \cos\bar{\theta}_{jik}]^2 \quad 8.$$

where,

$$\cos\theta_{jik} = \frac{\vec{r}_{ij} \cdot \vec{r}_{ik}}{r_{ij} r_{ik}}, \quad 9.$$

and B_{jik} is the strength of the interaction. ($\bar{\theta}_{jik}$ is a constant, 109.47° in the case of materials such as SiC, GaAs, and SiO_2 with tetrahedral units).

Another class of potentials, called the bond-order potentials, has been successfully used in simulations of covalently bonded systems (44). The general form of this potential is

$$E_b = \frac{1}{2}\left[\phi_{ij}^{(R)}(r_{ij}) - b_{ij}\phi_{ij}^{(A)}(r_{ij})\right], \quad 10.$$

where $\phi_{ij}^{(R)}(r)$ and $\phi_{ij}^{(A)}(r)$ represent the interatomic repulsion and the attractive

part due to bonding of valence electrons, respectively, and b_{ij} is a bond-order term. This potential has been used to describe bonding in silicon (45, 46), carbon (47), and germanium (48). The value of b_{ij} depends on the local coordination and bond angles. As the coordination increases, b_{ij} decreases and the bonds become weaker. A major drawback of this potential is that it is restricted to nearest neighbors only. Furthermore, the lack of charge transfer restricts it to predominately covalent materials.

Force Calculation

The most compute-intensive part of a MD simulation is the force calculation, which usually scales as N^2 where N is the number of atoms. For multimillion atoms, the cost of N^2 force computations is prohibitive. In the case of finite-ranged interatomic potentials, the cost can be reduced from O(N^2) to O(N) with the linked-list approach. In this method, the MD box is divided into smaller cells, and the force on an atom is from atoms in the same cell and those in nearest-neighbor cells (32, 49). Additionally, the multiple time step (MTS) method (50, 51) can be used to further speed up the force calculation. The MTS scheme exploits the fact that the force contribution from nearest-neighbor atoms varies more rapidly in time than the forces from second, third neighbors, etc. While the force from nearest neighbors is computed every time step, the contributions from the second, third, . . . neighbors are calculated after multiple time steps.

Parallel Implementation

MD simulations of dynamic fracture in real materials require large systems of the order of 10^6–10^9 atoms. It is very difficult to simulate such large systems on serial machines because of memory and speed constraints. However, on massively parallel computers billion atom simulations are currently feasible for real materials.

MD simulations have a great deal of inherent parallelism that can be exploited by domain decomposition, which is a divide-and-conquer scheme to distribute the computational load among the parallel processors in such a way that the interprocessor communication is minimal. Domain decomposition involves the division of the MD box into subsystems of equal volume, each of which is geometrically mapped to an individual processor (52, 53). Each processor then maintains information about the current positions and velocities of all the atoms that lie within its spatial domain. As the simulation proceeds, atoms may move across domain boundaries and, thus relevant data for these atoms are transferred to the new domains using message-passing interface calls (54). To calculate forces on atoms near the domain boundaries, various attributes of atoms in the boundary cells of neighboring domains are required. For this reason it is useful to define an extended node, as shown in Figure 3.

Load Balancing and Data Compression

Dynamic fracture simulations require adaptive domain decomposition to ensure that the computational load is distributed equally among the parallel processors because the number of atoms per processor can vary significantly as the crack propagates and branches and as pores open up in the system. A highly efficient load-balancing algorithm has been developed to address this problem (55). The algorithm is based on a curvilinear coordinate transformation, $\xi = x + u(x)$, that causes the computational space to shrink in regions of high workload density. Workloads are partitioned with a uniform three-dimensional mesh in the curved space, ξ (Figure 4*a*). The load-imbalance and communication costs are minimized as a functional of $u(x)$ using simulated annealing (Figure 4*b*). A multiresolution analysis based on wavelets leads to a compact representation of $u(x)$ and to fast convergence of the minimization procedure.

Massively parallel MD simulations generate considerable input and output data (*I/O*). For instance, a 1.5-billion-atom MD simulation produces 150 GB of data involving atomic species, positions, velocities, and stresses per frame. For scalable *I/O* of such huge datasets, we have designed a data-compression algorithm (56), which uses octree indexing and sorts atoms on a space-filling curve (Figure 5). By storing differences between successive atomic coordinates, the *I/O* requirement for the same error tolerance level reduces from $O(N \log N)$ to $O(N)$. An adaptive, variable-length encoding scheme is used to make the scheme tolerant to outliers. An order of magnitude improvement in the *I/O* performance is achieved for actual MD data with a user-controlled error bound.

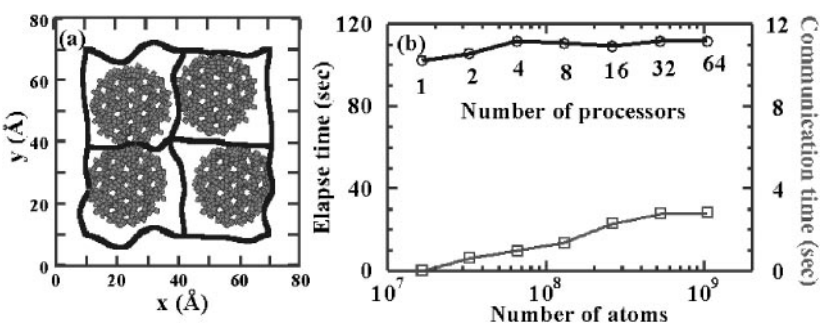

Figure 4 Shows the strategy and performance of an algorithm to balance computational load of the nodes on a parallel machine. (*a*) Regular domain decomposition in curvilinear space, which generates curved partition boundaries in the Euclidean space. (*b*) Performance of the load-balance algorithm on an IBM SP2 computer. The size of the system, *N*, scales linearly with the number of processors, *p*: $N =$ 16,301,600 *p*.

Visualization

Another difficulty with enormous MD datasets is the analysis and visualization of simulation results. Interactive exploration of such large datasets (walkthrough) is important for identifying and tracking atomic features that are responsible for macroscopic phenomena. An interactive and immersive virtual environment (VE) is highly desirable for large-scale MD simulations (Figure 6*a*). Algorithms have been designed to interact with multimillion atoms in VEs: Octree-based fast visibility culling to extract only the atoms in the viewer's field of view at runtime using octree data structures, thereby minimizing the data sent to the rendering system; and mutiresolution rendering to draw each atom at resolutions ranging from a point to a sphere using varying numbers of polygons according to the distance from the viewer (Figure 6*b*).

RESULTS

MD simulations have played a vital role in our understanding of mechanical behavior including crack propagation and failure in a variety of materials. With the current computing capabilities, the MD approach is able to provide valuable information at the crack tip and the surrounding region up to submicron length scales.

In MD simulations of dynamic fracture, the system is pre-cracked and then subjected to an external strain. Pre-cracking involves removing atoms from a specified region of the system. Subsequently, a conjugate gradient method is applied to relax the system. There are primarily two ways to strain a system: (*a*) An external strain is applied to the system by scaling the position of all the atoms every *n* time steps; (*b*) two thin layers of atoms, one at the top and the other at the bottom of the simulation box, are displaced in the direction of the applied strain (Figure 7) (this procedure is closer to experimental conditions). The strain is increased incrementally and between each increment the system is relaxed.

The boundaries of a MD box in a fracture simulation are also important because of the relatively small system size. Atoms at the boundaries are damped to avoid the reflection of stress waves emitted from the crack tip (57). Having described the setup of fracture simulations, we now discuss results of crack propagation in a variety of brittle materials.

Crack Branching in Graphine and GaAs

In recent years, there has been much interest in the role of instabilities in dynamic fracture in brittle solids (58–71). Both experimental (59–63) and theoretical (58, 64–72) studies reveal that when the crack tip speed reaches a certain fraction of the Rayleigh speed, c_R, the crack becomes unstable and forms microbranches that prevent the crack from reaching the terminal velocity c_R (73).

One of the best examples of microbranching in a MD simulation is found by Omeltchenko et al. in graphine (a single layer of graphite) containing 10^6 atoms (dimensions 150×200 nm) with dangling bonds terminated by hydrogen atoms

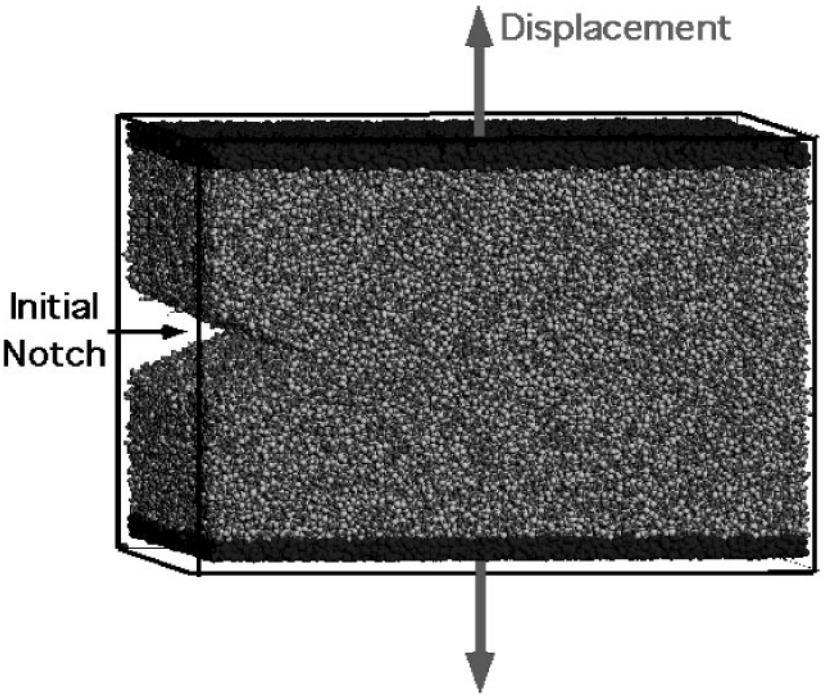

Figure 7 Shows how the strain is applied in a fracture simulation. An initial notch is created by removing atoms from a certain region. The strain is applied by displacing atoms in the top and bottom layers. Subsequently, the boundary layer atoms are frozen until the strain is further increased.

(72, 74, 75). Initially, the atoms in the sheet are in the *x-y* plane, but during the course of the simulation they are allowed to move in the *z*-direction as well. The simulations are performed at room temperature for two different crystallographic orientations (see Figure 8*a*,*b*): (*a*) G(1,1), where the *x* axis is parallel to some of the C-C bonds; and (*b*) G(0,1), where bonds make an angle of either 30° or 90° with the *x* axis.

For both orientations of the graphite sheet with an initial notch of length 3 nm, the crack does not propagate until the applied strain reaches a critical value of 12%. At the critical value, the crack grows and quickly reaches a terminal velocity of 6.2 km s^{-1} ($\sim$0.60 c_R). For G(1,1) orientation, the system undergoes cleavage fracture (see Figure 8*c*). The behavior is quite different in the case of G(1,0) (Figure 8*d*). After propagating for only 2 ps, the crack branches into two secondary cracks. Subsequently, more local branches sprout off the secondary cracks at an angle of 60°.

Microbranching in the G(1,0) orientation becomes more frequent at higher values of strain. At an applied strain of 16%, branches are almost equally spaced with a spacing of $\sim$20 nm, which provides an efficient mechanism for the dissipation of the strain energy in the system. In addition to the main crack branches, smaller

branches are visible with an average spacing of ∼5 nm. All branches are found to reach the same terminal speed.

As the crack-tip speed becomes a significant fraction of the Rayleigh speed, changes are observed in the angular dependence of the local stress distribution, $\sigma_{\theta\theta}$. The maximum local tension shifts from the crack plane ($\theta = 0^\circ$) to a plane inclined at an angle θ_m when the crack becomes unstable and undergoes bifurcations. The angular dependence of the local stress $\sigma_{\theta\theta}$ component before the onset of crack propagation and after the crack reaches the terminal velocity are shown in Figure 9*a*,*b*, respectively. The peak in the stress distribution shifts from $\theta = 0^\circ$ to $\theta_m \sim 30^\circ$ and the crack splits into two branches.

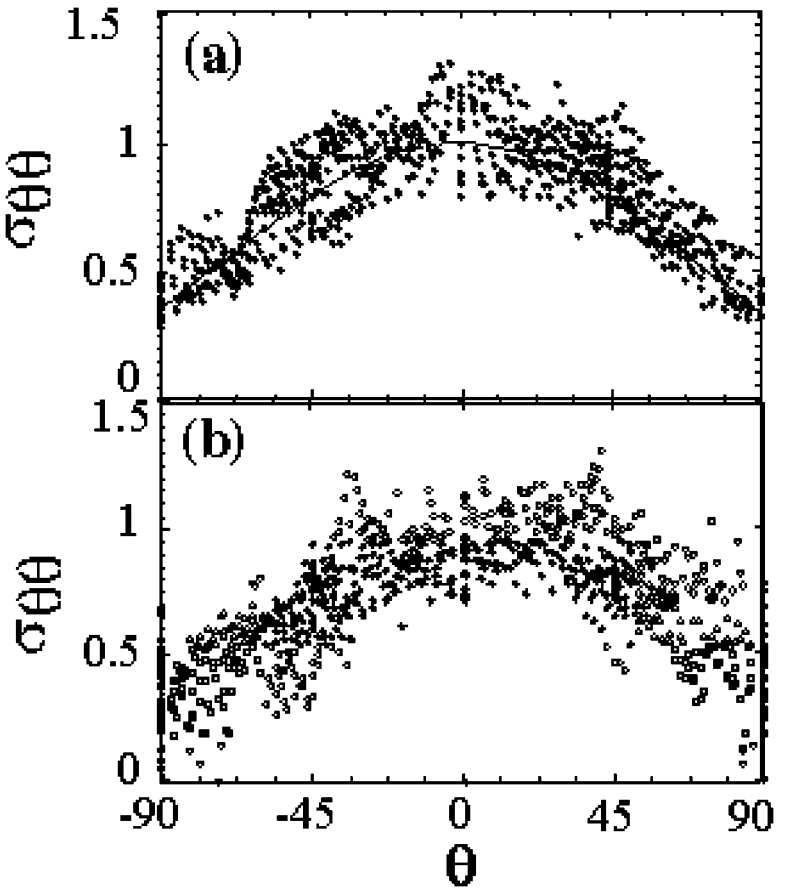

Figure 9 Plots of the angular dependence of the stress component, $\sigma_{\theta\theta}$, in graphine: (*a*) at the onset of crack propagation and (*b*) when the crack reaches the terminal velocity. The maximum in $\sigma_{\theta\theta}$ refers to the preferred direction of crack propagation. In (*a*) the maximum occurs at $\theta = 0^\circ$ indicating cleavage fracture, in (*b*) the peak shifts to $\theta \sim \pm 35^\circ$ along the branches of the crack.

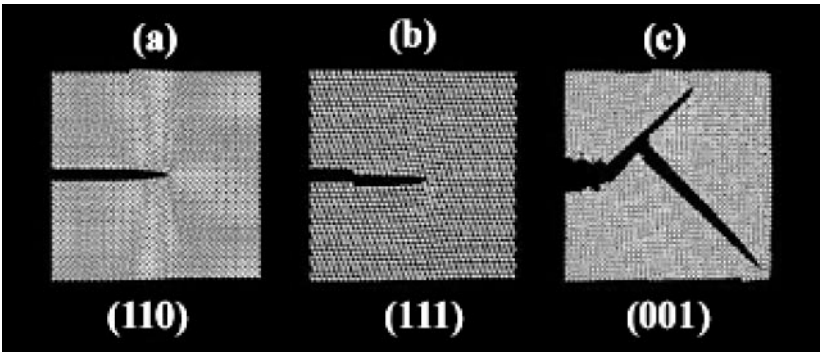

Figure 10 Snapshots of atomic configurations for brittle fracture in GaAs show: (*a*) cleavage fracture in the (110) orientation, (*b*) in the (111) orientation steps on the crack profile result from dislocation emission, and (*c*) crack branching in the (001) orientation.

Turning to three-dimensional brittle solids, H. Kikuchi, (unpublished data) has performed a set of 100-million-atom MD simulations to investigate crack propagation in three different crystallographic orientations of GaAs. They have calculated the mechanical-energy-release rate, G. In the (110) orientation, the onset of crack propagation is found at a critical value of $G_c = 1.4$ J m^{-2}. The system undergoes cleavage fracture, reaching a terminal velocity of 0.6 c_R (see Figure 10*a*), for the (111) orientation, dislocations are emitted from the crack tip (Figure 10*b*). As a result, the critical value of the mechanical-energy-release rate, $G_c = 1.7$ J m^{-2}, is higher. This is within the range of experimental values (1.52–1.72 J m^{-2}). Another set of simulations involves the (001) orientation (Figure 10*c*), where crack branching is observed, and the value of G_c is found to be 2.0 J m^{-2}. H. Kikuchi has also investigated the influence of temperature on crack propagation in GaAs (private communication) and finds that the mechanical-energy-release rate is much larger at higher temperatures because of dislocation emission and other dissipative effects.

Cracks and Nanopores in Nanophase Ceramics

In addition to branching, another important dissipation mechanism involves the formation of nanopores and coalescence with cracks. This mechanism is extensively found in nanophase ceramics—a class of tough ceramics that does not break abruptly. In the mid-1980s, it was discovered that ceramics can be made ductile when they are synthesized by sintering nanometer-size particles. [Metallic systems comprising nanometer-size particles display significant increase in the yield strength (76).] Enhanced ductility of these so-called nanophase ceramics is attributed to grain boundaries having a large fraction of atoms (77, 78). However, there is little quantitative understanding of the relationship between the intergranular structure and mechanical properties of nanophase materials.

Omeltchenko et al. have studied the effect of ultrafine microstructures on the mechanical strength of silicon nitride using a million-atom MD simulation (79). A well-consolidated nanophase material is prepared by sintering 6-nm-sized Si_3N_4 nanoparticles (79, 80). Initially, the MD box contains 108 nanoparticles at random positions and with random orientations. Periodic boundary conditions are imposed and the simulation is run at constant pressure using the Parinello-Rahman (81) variable-shape MD approach. The system is first thermalized at 2000 K under zero pressure and then consolidated by successively increasing the pressure to 1, 5, 10, and 15 GPa. At each value of the external pressure, the system is sintered for several thousand time steps. Subsequently, the consolidated system is slowly cooled down to 300 K. After reaching room temperature, the external pressure is gradually reduced to zero. Subsequently, the structure of the nanophase system is analyzed by calculating, for example, partial and total pair-distribution functions and bond-angle distributions. The simulations reveal that intergranular regions are amorphous and structurally similar to bulk amorphous Si_3N_4 at the same mass density.

A notch is inserted in the consolidated nanophase system at room temperature and the system is subjected to uniaxial tensile strain. The motion of the crack is followed by partitioning the simulation box into voxels of sizes 0.4 nm. Adjacent empty voxels define a pore, and pores connected to the notch define the crack in the system. Figure 11*a* shows a snapshot of pores taken 10 ps (5% of strain) after the notch is inserted in Si_3N_4. The crack advances slightly and local branches develop near the notch. These branches tend to arrest the motion of the crack front, and further crack growth is only possible at a higher value of strain. The strain is further increased by 1% over 4 ps and the system is relaxed for 10 ps. This procedure is repeated until the system fractures. Figure 11*b* shows that when the strain is increased to 11%, the crack advances significantly and coalesces with pores at the center of the sample. Pores and amorphous intergranular regions cause the crack to meander and form a complex branched structure. Multiple crack branching provides an efficient mechanism for energy dissipation, which prevents further crack propagation. Figure 11*c* also shows a secondary crack in the upper-left corner of the box. After the strain reaches 14%, the primary and secondary cracks coalesce without completely fracturing the system. There are atomic links across the crack surfaces, and the material around them is still connected. It takes an applied strain of 30% to completely fracture the nanophase system (Figure 12*b*). We observe that fracture proceeds primarily along intergranular regions. The nanoparticles adjacent to the crack rearrange themselves to accommodate large applied strain. This relative motion of nanoparticles is accompanied by plastic deformation of amorphous intergranular regions.

Omeltchenko et al. have also performed MD simulation of fracture in α-crystalline silicon nitride using the same geometry and size as in the case of the nanophase system (79). In the crystalline case, cleavage fracture is observed at a strain of only 3% (see Figure 12*a*).

The strain energy per unit area for fracture in crystalline and amorphous samples has also been estimated. For the nanophase system, the fracture energy is 24 J m^{-2}, whereas for the crystal, the value is 4 J m^{-2}. In nanocrystalline Si_3N_4 the complex branched structure and plastic deformation provide efficient mechanisms for energy dissipation, which makes the system much tougher than crystalline Si_3N_4.

L. Van Brutzel (unpublished data) has investigated crack propagation and fracture in nanostructured amorphous silica (n-SiO_2) and bulk amorphous silica (a-SiO_2) at room temperature and high temperature. Amorphous silica was obtained by quenching molten SiO_2. The n-SiO_2 system was prepared by sintering amorphous SiO_2 nanoparticles cut out of bulk a-SiO_2. The high-temperature bulk and nanophase silica samples were obtained by heating the room-temperature systems to 1000 K and relaxing them for 50,000 Δt. Subsequently, a 4 $\times$ 5 nm notch was inserted in each of the four samples (bulk and nanophase at 300 K and 1000 K), the systems were relaxed, and then subjected to uniaxial strains in the *x*-direction.

Snapshots of cracks and nanopores in bulk amorphous and nanophase silica are shown in Figures 13 and 14. In both systems, the crack propagates by growth and coalescence of pores. The number of pores and their nucleation vary with the system and temperature. In bulk SiO_2 at 1000 K, nanopores open up everywhere in the sample even far ahead of the crack tip. This is not the case at room temperature, where the pores appear 5 nm ahead of the crack tip in the plane of propagation. The onset of crack propagation at 1000 K is at a much higher strain ($\sim$7%) than at room temperature ($\sim$3%). Crack propagations in nanophase silica at 300 and 1000 K are quite similar; cracks meander along interparticle boundaries and coalesce with pores to cause intergranular fracture at a strain of $\sim$7%.

Ceramic Matrix Nanocomposite

In addition to sintering of ceramics nanoparticles, another approach to designing tough ceramics is to embed SiC fibers in a Si_3N_4 matrix (82). The basic motivation behind fabricating materials of this type is to embed fibers of a hard material into a hard ceramic host with a weak interface between the host material and the fiber. The fibers are coated to have the desired weak interface with the matrix.

Recently, A. Nakano (private communication) performed a 1.5-billion-atom MD simulation to investigate fracture in silicon nitride reinforced with silicon carbide fibers (fiber diameter 3 nm, length 24 nm) (Figure 15). In order to simulate the effect of a glassy phase, which lubricates the fiber-matrix interfaces, silicon carbide fibers are coated with an amorphous silica layer of thickness 0.5 nm. The effects of interphase structure and residual stresses on fracture toughness have also been investigated. Immersive visualization of these simulations reveals a rich diversity of atomic processes, including fiber rupture, frictional pullout, and emission of molecular fragments, which must all be taken into account in the design of tough ceramic composites.

Scaling Properties of Cracks and Fracture Surfaces

The different fracture mechanisms discussed above give rise to fracture surfaces that have certain common features. In 1984, Mandelbrot et al. (83) showed that fracture surfaces in heterogeneous materials are self-affine objects, i.e., they are invariant with respect to an anisotropic dilatation $(x, y, z) \rightarrow (\lambda x, \lambda y, \lambda^{\zeta} z)$, where ζ is called the roughness exponent. This self-affine behavior ranges between the precision of the experimental probe and a certain correlation length, ξ, which is material dependent. Measurements in brittle and ductile materials, such as steel, ceramics, glass, wood, and polymers, reveal the same value of the roughness exponent using different experimental techniques (84–89). Bouchaud et al. have observed two roughness exponents, one at small length scales, $\zeta \sim 0.5$, and a second exponent, $\zeta \sim 0.8$, at larger length scales separated by a crossover length, ξ_c (90, 91), which depends strongly on microstructures in the material. It has also been determined that the crossover length shifts to smaller values as the crack velocity increases.

Vashishta et al. have performed large MD simulations to investigate the morphology of fracture surfaces in crystalline, amorphous, and nanophase Si_3N_4 (79, 92). In crystalline Si_3N_4, the crack cleaves through the film with a steady velocity of 3.1 km s^{-1}, which is half the Rayleigh speed in this material. A snapshot of cracks in amorphous Si_3N_4 is shown in Figure 16*a*. In this system, the behavior is quite different: Voids appear ahead of the crack tip and they grow to

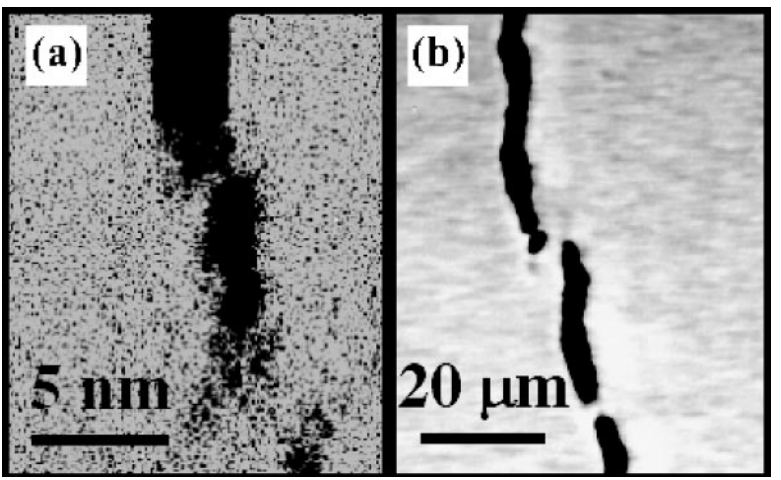

Figure 16 Morphology of fracture surfaces: (*a*) Snapshot of a MD configuration showing the crack and nanopores (*dark*) and atoms (*light*) in an amorphous Si_3N_4 film. Initially the crack propagates straight. Voids in front of the crack coalesce with each other and form a second crack. (*b*) Scanning electron microscropy in situ experiment in titanium-aluminide based alloy shows similar crack-and-void formation (89).

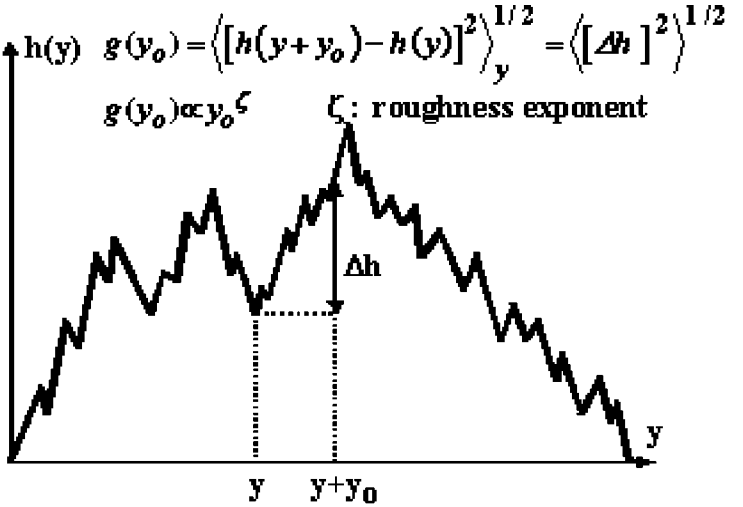

Figure 17 Schematic of a fracture surface profile. The height-height correlation function, $g(y)$, is expected to behave as y^{ζ}, where ζ is the roughness exponent.

form a secondary crack that coalesces with the main crack. This pattern in MD simulations is similar to the experimental observation in a Ti_3Al-based alloy (see Figure 16*b*), even though the length scales are significantly different and fracture is quasi-static instead of dynamic (93).

The roughness exponent of fracture profiles $h(y)$ is determined from the height-height correlation function $g(y_o)$ (see Figure 17):

$$g(y_o) = \langle [h(y + y_o) - h(y)]^2 \rangle^{1/2}. \qquad 11.$$

The bracket $\langle \cdots \rangle$ denotes an average over y. For self-affine behavior of the fracture surface, $g(y_o)$ scales with y_o as,

$$g(y_o) \propto y_o^{\zeta}, \qquad 12.$$

where ζ is the roughness exponent. In three dimensions one can define three different profiles—$h_y(z)$, $h_x(z)$, and $h_x(y)$—yielding three different roughness exponents (see Figure 18). Results for the computed out-of-plane roughness exponent (corresponding to the profile $h_x(z)$; see Figure 18) for nanostructured Si_3N_4 are shown in Figure 19*a*. There are two well-defined self-affine regions. The roughness exponent is calculated to be $\zeta_\perp = 0.58 \pm 0.12$ below 6 nm (the nanoparticle size) and $\zeta_\perp = 0.84 \pm 0.12$ beyond 6 nm. A similar study in amorphous Si_3N_4 gives roughness exponents close to these results, although the crossover length is smaller ($\zeta_c = 2.5$ nm, typical size of the cavity). Detailed analysis reveals that the smaller exponent corresponds to slow crack propagation inside microcracks,

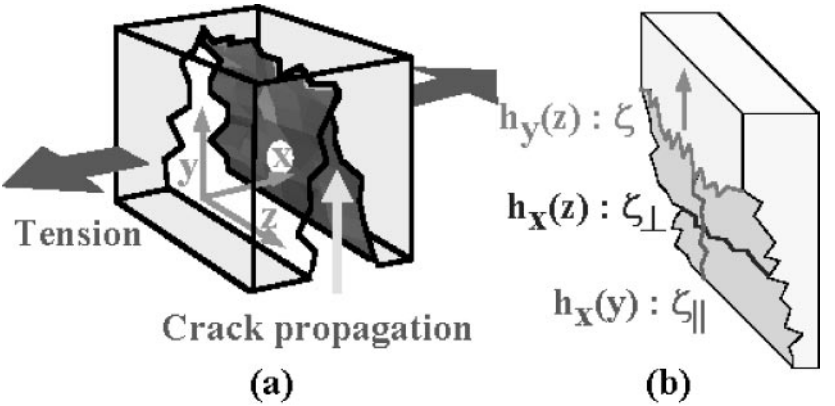

Figure 18 (*a*) Schematic of fracture surfaces. The applied strain is along the *x* axis. (*b*) Three distinct roughness exponents are shown: ζ is in-plane roughness exponent corresponding to the profile $h_y(z)$, $\zeta_\perp$ is the out-of-plane roughness exponent perpendicular to the direction of the crack propagation for the profile $h_x(z)$, and $\zeta_\parallel$ is the out-of-plane roughness exponent parallel to the direction of the crack propagation for the profile $h_x(y)$.

whereas the larger exponent is due to coalescence of microcracks with the primary crack, which causes rapid propagation. The in-plane roughness exponent for nanostructured Si_3N_4 has also been calculated. The best fit to the corresponding height-height correlation gives $\zeta_\parallel = 0.57 \pm 0.08$ (see Figure 19*b*); experimental values range between 0.5 and 0.65.

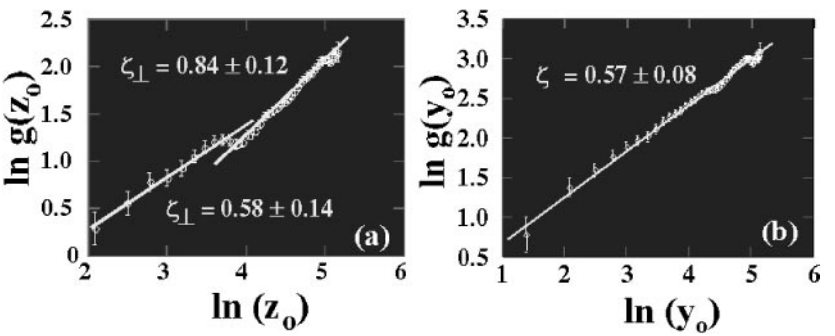

Figure 19 Log-log plots of the height-height correlation function for fracture surfaces in nanophase Si_3N_4. (*a*) For the out-of-plane profile $h_x(z)$ (see Figure 18), the solid curves represent the best fit, $g(z) \propto z^\zeta$, with $\zeta_\perp = 0.58 \pm 0.14$ for $z_o < \xi_c$ ($\sim$2.5 nm), and $\zeta_\perp = 0.84 \pm 0.12$ for $z_o > \xi_c$. (*b*) For the in-plane profile $h_y(z)$, the solid curve represents the best fit, $g(z) \propto z^\zeta$, with $\zeta = 0.57 \pm 0.08$. For the two profiles, nearly the same roughness exponents are found experimentally in a variety of other materials.

Omeltchenko et al. have performed fractal analyses of branched fracture profiles in graphine for the G(1,0) orientation under 12 and 16% strains (72). The roughness exponents have been computed from the height-height correlation function and also from the return probability histogram. A single branch from the fracture profile is picked so that the computed function involves only correlations within the same branch. Over two orders of magnitude, these data are well described by a roughness exponent $\zeta = 0.41 \pm 0.05$. For the same crack front, the direction-dependent return probability histogram $P(r)$ has also been calculated. In this case, the average is taken over the whole fracture profile, and the correlations are no longer restricted to the same branch. Above a crossover length of about 5 nm, the data can be fitted to $P(r) \sim r^{-\zeta}$ with $\zeta = 0.71 \pm 0.10$. This is in good agreement with careful experimental studies of fracture in two-dimensional systems (paper, wood), which yield $\zeta = 0.68 \pm 0.004$ (94, 95). The larger roughness exponent corresponds to "interbranch" correlations, which are dominant above the crossover length. Similar scaling behavior is observed for the fracture profile obtained at 12% strain. However, because of larger spacing between branches, the crossover length shifts from 5 to 15 nm. In these simulations, the crossover results from crack branching. Intrabranch fracture corresponds to the smaller exponent ($\zeta = 0.4$), whereas interbranch correlations lead to a higher roughness exponent ($\zeta = 0.7$).

MULTIPLE LENGTH SCALE SIMULATIONS

Although MD is an excellent simulation technique to study crack dynamics, a different approach is needed to explicitly incorporate bond breakage and bond formation processes and to extend the simulation to mesoscopic and macroscopic length scales. Appending FE to MD incorporates larger length scales (26–28), whereas DFT-based calculations embedded in MD are able to explicitly account for bond formation and bond breakage. Figure 20 depicts the regions of applicability of each method in a fracture simulation.

MD and FE Coupling

In the hybrid MD/FE scheme, the system is divided into a MD region, a continuum described by the FE approach, and an overlapping MD/FE region called the handshake (HS) region (Figure 21*a*). The FE method numerically solves the equations of elasticity theory on a computational grid with local deformations for the FE nodes. Using an appropriate constitutive relation, the continuum problem may thus be cast into a set of coupled ordinary differential equations that describe the time evolution of the nodes. Often, the lumped mass approximation with the diagonal mass matrix is used in the dynamical FE approach. In the HS region, the FE nodes coincide with atoms, and the Hamiltonian of the hybrid atoms/nodes is taken to be a weighted average of MD and FE Hamiltonians (28).

Lidorikis et al. have implemented this hybrid method for a three-dimensional block of crystalline silicon and checked the response of the system after a projectile hits a section of the MD box (96). Color-coded absolute values of displacements

of Si atoms and nodes from their equilibrium positions at three different instants of time are shown in Figure 21*b*. No significant reflections are observed as the displacement wave travels from the MD through the HS into the FE region. This demonstrates that the coupling between the MD and FE regions is seamless.

Coupling MD and QM Methods

Quantum mechanics (QM) is employed in regions where chemical reactions and bond breaking need to be described explicitly. The QM method discussed here is based on the density functional theory (DFT). In the region where QM information is needed, both MD and DFT methods are used to calculate the energy of a cluster. In DFT, hydrogen atoms terminate the dangling bonds of atoms at the cluster boundary. The total energy of the system is calculated from

$$E_{total} \cong E_{MD}^{system} + E_{DFT}^{cluster} - E_{MD}^{cluster}, \qquad 13.$$

where E_{MD}^{system} and $E_{MD}^{cluster}$ are the energies of the entire system and of the atomic cluster, respectively, calculated with MD, whereas $E_{DFT}^{cluster}$ refers to the energy of the cluster calculated with DFT.

Ogata et al. have implemented this hybrid DFT and MD scheme (97) and tested it on the oxidation of silicon. Figure 22 shows two snapshots of the energy transfer within the system. The energy released from the dissociation of an oxygen molecule propagates seamlessly from the QM to the MD region.

Coupling FE/MD/QM

Abraham et al. carried out the first fracture simulation using all three methodologies (28). Inside a slab of Si described by FE is embedded an atomic region described by MD. In the middle of the MD region, a microcrack was introduced and an atomic cluster, treated quantum mechanically via the tight-binding (TB) method, was defined at each corner of the microcrack. As the crack advances in time, an adaptive TB scheme is used to follow the crack tip. It is found that stress waves from the crack tip propagate seamlessly without reflections from the QM to FE region. Ogata et al. have used a multiscale scheme combining the DFT, MD, and FE approaches (97) to investigate the dissociation of an oxygen molecule on the Si(111) surface (Figure 23). The dissociation energy is transferred from the DFT region to the MD region and then to the FE region with no noticeable reflections, demonstrating a seamless coupling of all three approaches over disparate length scales.

CONCLUSIONS

This review has focused on MD simulations of dynamic fracture in a variety of brittle materials. Results have been presented for (*a*) graphine; (*b*) crystalline gallium arsenide; (*c*) bulk and nanophase amorphous silica; (*d*) crystalline, amorphous,

and nanophase silicon nitride; and (*e*) a nanocomposite consisting of silica-coated silicon carbide fibers embedded in a silicon nitride matrix. Reliable interatomic potentials, validated by comparison with various experimental measurements, have been used in simulations ranging from 10^6 to 10^9 atoms. All simulations are based on highly efficient algorithms that scale linearly with the number of atoms. The algorithms also map very well on parallel machines: Interprocessor communication takes only 3% of the execution time. Furthermore, highly efficient data compression algorithms have been developed for scalable *I/O*.

The first set of simulations pertained to crack branching in a million-atom graphine system. For the G(1,1) orientation, where some of the C-C bonds are parallel to the applied strain, the system undergoes cleavage fracture with a terminal velocity ~0.6 times the speed of Rayleigh waves, c_R. (Experiments reveal that cleavage fracture in many brittle materials occurs at the same terminal speed $0.6\,c_R$.) In the perpendicular orientation G(1,0) the crack splits into several branches, which appear at regular intervals that vary with the applied strain. The stress-distribution analysis reveals a preferential cleavage plane in graphine, and these results are in accordance with the theory of elasticity.

A set of 100-million-atom MD simulations was carried out to investigate dynamic fracture in various crystalline orientations of GaAs. In the (110) orientation, fracture is cleavage-like, whereas crack branching and dislocation emission have been observed in (111) and (001) orientations, respectively. The measured critical energy-release rate compares well with the available experiment values.

Various modes of crack propagation at the atomic scale have been found in crystalline, amorphous, and nanophase Si_3N_4. In the amorphous case, the crack propagates by growth and coalescence of voids that open up ahead of the crack tip. In crystalline Si_3N_4, the crack propagates by cleavage, and all the strain energy is dissipated at the crack tip. The fracture in nanophase Si_3N_4 is mainly intergranular: The crack meanders around nanoparticles creating multiple branches and secondary cracks, which result in a large strain-energy dissipation. As a result, the nanophase system is able to sustain an order of magnitude larger external strain than its crystalline counterpart.

Amorphous and nanophase SiO_2 also exhibit similar behavior. In these materials, the influence of temperature has also been studied. In a-SiO_2, the strain corresponding to the onset of crack propagation increases with temperature, whereas in n-SiO_2, the onset is insensitive to temperature.

The largest and the most complex dynamic fracture simulation we have performed involves a 1.5-billion-atom nanocomposite consisting of silica-coated silicon carbide fibers in a silicon nitride matrix. Immersive visualizations of these simulations reveal that frictional fiber pullout allows significant dissipation of the external strain energy, thereby making the nanocomposite much tougher than its constituent materials.

The morphology of fracture surfaces has been examined in amorphous Si_3N_4 and nanophase Si_3N_4. Both in-plane and out-of-plane fracture profiles are well characterized by roughness exponents. The in-plane roughness exponent in nanophase

Si_3N_4 is $\zeta_{\parallel} \approx 0.57$. Experimental measurements in various systems range between 0.5 and 0.65. The out-of-plane fracture profile reveals two roughness exponents over two decades of length scales: $\zeta_{\perp} \approx 0.5$ and $\zeta_{\perp} \approx 0.8$, below and above a certain crossover length, respectively. The crossover length depends on the microstructure and crack velocity. These results are in excellent agreement with experimental measurements. From simulations, we have determined that the smaller exponent corresponds to slow crack propagation inside microcracks, whereas the larger exponent corresponds to rapid crack propagation involving coalescence with microcracks.

Finally, novel multiscale simulation approaches have emerged recently for investigating dynamic fracture more realistically than afforded by the MD approach alone. The most promising approach combines MD with electronic structure calculations in the framework of the density function theory (DFT) to explicitly incorporate bond-breakage and bond-formation processes. The combined DFT/MD approach has also been seamlessly integrated with the finite-element method so that the boundaries of the system are far removed from any process zone.

Although the DFT/MD/FE integration has successfully bridged length scales for fracture simulations, the disparate time scales in atomic and macroscopic simulations present a daunting problem. This is the next frontier in dynamic-fracture simulations.

ACKNOWLEDGMENTS

We thank Drs. Elisabeth Bouchaud, Hideaki Kikuchi, and Sanjay Kodiyalam for helpful discussions. This work is supported by NSF-FRG (DMR 0085344), DOE (DE-FG02-96ER45570), AFOSR (F49620-99-1-0250), NASA (NCC2-5320), LEQSF, and a Challenge award from DoD HPCMO.

The *Annual Review of Materials Research* is online at http://matsci.annualreviews.org

LITERATURE CITED

1. Griffith AA. 1920. *Philos. Trans.* 221A:163
2. Lawn B. 1993. The Griffith concept. In *Fracture of Brittle Solids-Second Edition*. ed. EA Davis, IM Ward, pp. 1–50. Cambridge, UK: Cambridge Univ. Press 2nd ed.
3. Anderson TL. 1995. *Fracture Mechanics Fundamentals and Applications*, pp. 31–99. Boca Raton, FL: CRC Press. 2nd ed.
4. Inglis CE. 1913. *Trans. Inst. Naval Archit.* 55:219
5. Irwin GR. 1956. *Sagamore Res. Conf. Proc.* 2:289
6. Westergaard HM. 1939. *J. Appl. Mech.* 6:49
7. Sneddon IN. 1946. *Proc. R. Soc. London Ser. A* 187A:229
8. Irwin GR. 1957. *J. Appl. Mech.* 24:361
9. Williams ML. 1957. *J. Appl. Mech.* 24:109
10. Barenblatt GI. 1962. *Adv. Appl. Mech.* 7: 55
11. Rice JR. 1968. *J. Appl. Mech.* 35:379
12. Beale PD, Srolovitz DJ. 1988. *Phys. Rev. B* 37:5500
13. Li YS, Duxbury PM. 1988. *Phys. Rev. B* 38:9257

14. Thomson R, Zhou SJ, Carlsson AE, Tewary VK. 1992. *Phys. Rev. B* 46:10613
15. Hoenberg P, Kohn W. 1964. *Phys. Rev.* 136: 864
16. Kohn W, Sham LJ. 1965. *Phys. Rev.* 137: 1697
17. Kohn W, Sham LJ. 1965. *Phys. Rev.* 140(4A):1133
18. Car R, Parrinello M. 1985. *Phys. Rev. Lett.* 55(22):2471
19. Slater JC, Koster GF. 1954. *Phys. Rev.* 94: 1498
20. Harrison WA. 1986. *Phys. Rev. B* 34:2787
21. Sutton AP, Finnis MW, Pettifor DG, Otha Y. 1988. *J. Phys. C Solid State* 21:35
22. Marx DD, Parrinello M. 1996. *J. Chem. Phys.* 104:4077
23. Tuckerman ME, Marx DD, Klein ML, Parrinello M. 1997. *Science* 275:817
24. Eichinger M, Tavan P, Hutter J, Parrinello M. 1999. *J. Chem. Phys.* 110:10452
25. Kowada Y, Ellis DE. 2001. *Adv. Quantum Chem.* 37:271
26. Mullins M, Dokainish MA. 1982. *Philos. Mag. A* 46:771
27. Kohlhoff S, Gumbsch P, Fischmeinster HF. 1991. *Philos. Mag. A* 64:851
28. Abraham FF, Broughton JQ, Bernstein N, Kaxiras E. 1998. *Comput. Phys.* 12:538
29. Lidorikis E, Bachlechner ME, Kalia RK, Vashishta P, Voyiadjis GZ. 2001. *Phys. Rev. Lett.* 87:086104
30. Rudd RE, Broughton JQ. 2000. *Phys. Stat. Solidi B* 217:251
31. Tadmor EB, Ortiz M, Phillips R. 1996. *Philos. Mag. A* 73:1529
32. Allen MP, Tildesley DJ. 1987. *Computer Simulation of Liquids*. Oxford, UK: Clarendon
33. Verlet L. 1967. *Phys. Rev.* 159:98
34. Swope WC, Andersen HC, Berens PH, Wilson KR. 1982. *J. Chem. Phys.* 76:637
35. Huggins ML, Mayer JE 1933. *J. Chem. Phys.* 1:643
36. Vashishta P, Kalia RK, Rino JP, Ebbsjö I. 1990. *Phys. Rev. B* 41:12197
37. Daw MS, Baskes MI. 1984. *Phys. Rev B* 29:6443
38. Foiles SM, Baskes MI, Daw MS. 1986. *Phys. Rev. B* 33:7983
39. Tersoff J. 1988. *Phys. Rev. B* 37:6991
40. Brenner DW. 1990. *Phys. Rev. B* 42:9458
41. Stillinger FH, Weber TA. 1985. *Phys. Rev. B* 31:5262
42. Vashishta P, Kalia RK, Rino JP, Ebbsjö I. 1995. *Phys. Rev. Lett.* 75(5):858
43. Loong CK, Vashishta P, Kalia RK, Ebbsjö I. 1995. *Europhys. Lett.* 31:201
44. Abell GC. 1985. *Phys. Rev. B* 31:6184
45. Tersoff J. 1986. *Phys. Rev. Lett.* 56:632
46. Tersoff J. 1988. *Phys. Rev. B* 37:6991
47. Tersoff J. 1988. *Phys. Rev. Lett.* 61:2879
48. Tersoff J. 1989. *Phys. Rev. B* 39:5566
49. Nakano A, Vashishsta P, Kalia RK. 1993. *Comp. Phys. Commun.* 77:303
50. Streett WB, Tildesley DJ, Saville G. 1978. *Mol. Phys.* 35:639
51. Humphreys DD, Friesner RA, Berne BJ. 1994. *J. Phys. Chem.* 153:250
52. Nakano A, Vashishsta P, Kalia RK. 1994. *Comp. Phys. Commun.* 83:197
53. Rapapport DC. 1995. *The Art of Molecular Dynamics Simulation*. Cambridge, UK: Cambridge Univ. Press
54. Gropp W, Lusk E, Skjellum A. 1994. *Using MPI Portable Parallel Programming the Message-Passing Interface*, pp. 21–153. Cambridge, MA: MIT Press
55. Fox GC, Williams RD, Messina PC. 1994. *Parallel Computing Work*. San Francisco: Kaufmann
56. Omeltchenko A, Campbell TJ, Kalia RK, Liu X, Nakano A, et al. 2000. *Comp. Phys. Commun.* 131:78
57. Holland D, Marder M. 1999. *Adv. Mater.* 11:793
58. Nakano A, Kalia RK, Vashishta P. 1995. *Phys. Rev. Lett.* 75:3138
59. Sharon E, Gross SP, Fineberg J. 1996. *Phys. Rev. Lett.* 76:2117
60. Sharon E, Gross SP, Fineberg J. 1995. *Phys. Rev. Lett.* 74:5096
61. Fineberg J, Gross SP, Marder M, Swinney HL. 1991. *Phys. Rev. Lett.* 67:457
62. Fineberg J, Gross SP, Marder M, Swinney HL. 1992. *Phys. Rev. Lett.* 45:5146

63. Gross SP, Fineberg J, Marder M, MacCormick WD, Swinney HL. 1993. *Phys. Rev. Lett.* 71:3162
64. Langer JS. 1992. *Phys. Rev. A* 46:3133
65. Ravi-Chandar K, Knauss WG. 1994. *Int. J. Fracture* 26:141
66. Ching ESC. 1994. *Phys. Rev. E* 49:3382
67. Marder M, Fineberg J. 1996. *Phys. Today* 49:24
68. Marder M, Liu X. 1993. *Phys. Rev. Lett.* 71:2417
69. Marder M, Gross S. 1995. *J. Mech. Phys. Solids* 43:1
70. Abraham FF, Brodbeck D, Rafey RA, Rudge WE. 1994. *Phys. Rev. Lett.* 73:272
71. Abraham FF. 1996. *Phys. Rev. Lett.* 77:869
72. Omeltchenko A, Yu J, Kalia RK, Vashishta P. 1997. *Phys. Rev. Lett.* 78:2148
73. Yoffe EH. 1951. *Philos. Mag.* 42:739
74. Yu J, Omeltchenko A, Kalia RK, Vashishta P, Brenner DW. 1996. *Mater. Res. Soc. Proc.* 409:11
75. Vashishta P, Kalia RK, Li W, Nakano A, Omeltchenko A, et al. 1996. *Curr. Opin. Solid State Mater. Sci.* 1:853–63
76. Karch J, Birringer R, Gleiter H. 1987. *Nature* 330:556
77. Siegel RW. 1992. Nanophase materials: structure-property correlation. In *Materials Interfaces: Atomic-level Structure and Properties*. ed. D Wolf, S Yip, pp. 431–60. London: Chapman Hall.
78. Stern EA, Siegel RW, Newville M, Sanders PG, Haskel D. 1995. *Phys. Rev. Lett.* 75:3874
79. Kalia RK, Nakano A, Omeltchenko A, Tsuruta K, Vashishta P. 1997. *Phys. Rev. Lett.* 78:2144
80. Kalia RK, Nakano A, Tsuruta K, Vashishta P. 1997. *Phys. Rev. Lett.* 78:689
81. Parinello M, Rahman A, 1981. *J. Appl. Phys.* 52:7182
82. Evans AG. 1990. *J. Am. Ceram. Soc.* 73:187
83. Mandelbrot BB, Passoja DE, Paullay AJ. 1984. *Nature* 308:721
84. Dauskardt RH, Haubensak F, Ritchie RO. 1990. *Acta. Metall. Mater.* 38:143
85. Melcholsky JJ, Passoja DE, Feinberg-Ringel KS. 1989. *J. Am. Ceram. Soc.* 72:60
86. Måløy KJ, Hansen A, Hinrichsen El, Roux S. 1992. *Phys. Rev. Lett.* 68:213
87. Bouchaud E, Lapasset G, Planès J, Navéos S. 1993. *Phys. Rev. B* 48:2917
88. Schmittbuhl J, Gentier S, Roux S. 1993. *Geophys. Res. Lett.* 20:8
89. Guilloteau E, Charrue H, Creuzet F. 1996. *Europhys. Lett.* 34:549
90. Daguier P, Hénaux S, Bouchaud E, Creuzet F. 1996. *Phys. Rev. E* 53:5637
91. Bouchaud E. 1997. *J. Phys. Condens. Matter* 9:4319
92. Vashishta P, Nakano A, Kalia RK, Ebbsjö I. 1996. *Mater. Sci. Eng. B* 37:56
93. Bouchaud E, Paun F. 1999. *Comput. Sci. Eng.* 1:32
94. Engoy T, Maloy KJ, Hansen A, Roux S. 1994. *Phys. Rev. Lett.* 73:834
95. Kertész J, Horváth V, Weber F. 1993. *Fractals* 1:67
96. Lidorikis E, Bachlechner ME, Kalia RK, Voyiadjis G, et al. 2001. *Mater. Res. Symp. Proc.* 653:Z9.3
97. Ogata S, Lidorikis E, Shimojo F, Nakano A, Vashishta P, et al. 2001. *Comp. Phys. Commun.* 138:143

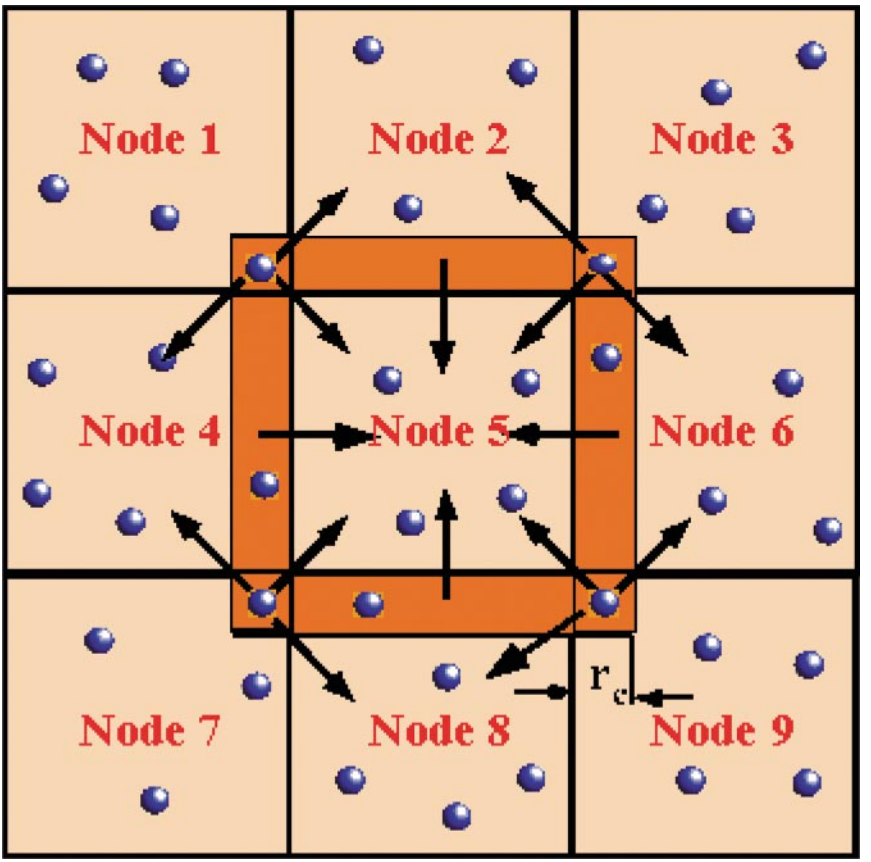

Figure 3 Domain decomposition on a parallel computer. Nodes of the parallel machine are arranged in two dimensions. In this illustration, the MD system is decomposed into *p* subsystems of equal volume, where *p* is the number of nodes. Atoms in a node interact among themselves and also with atoms in surrounding nodes. Thus communication between nodes is necessary to determine force contributions from atoms on other nodes and to transfer atoms to other nodes when they cross node boundaries. In the figure, atoms of node 5 interact with atoms of surrounding nodes within a certain distance r_c from the boundaries (*dark orange region*), where r_c is the range of the interatomic potential. *Arrows* indicate message-passing directions between nodes. The node boundaries plus the dark orange region is referred to as the extended node.

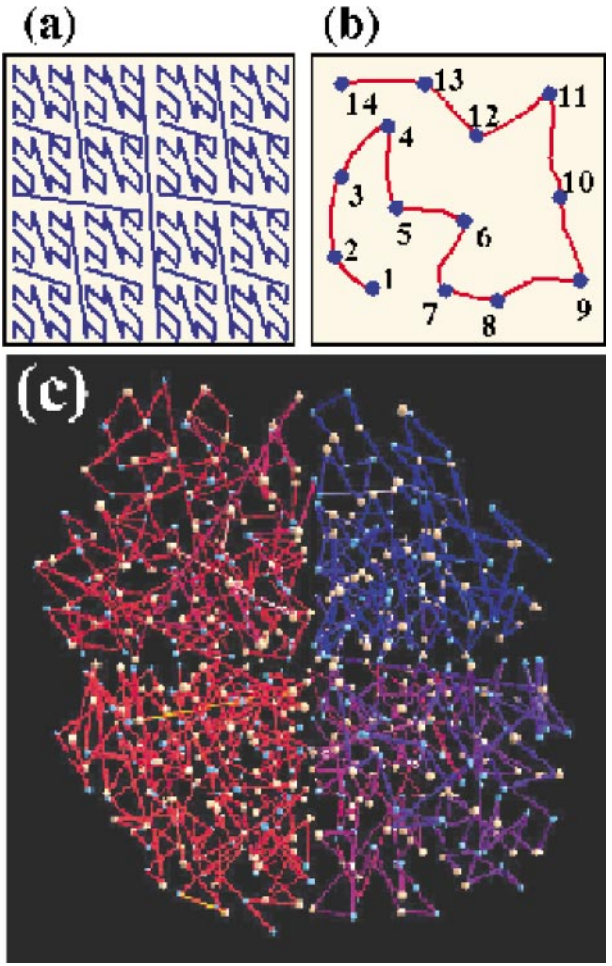

Figure 5 Illustration of a data-compression algorithm based on octree indexing of a space-filling curve. As an example, the curve shown in (*a*) maps the two-dimensional space into a sequential list, which preserves spatial proximity of consecutive list elements; (*b*) atoms are sorted along the space-filling curve and only relative positions are stored; and (*c*) a three-dimensional space-filling curve color coded from *red* (the head of the list) to *blue* (the tail).

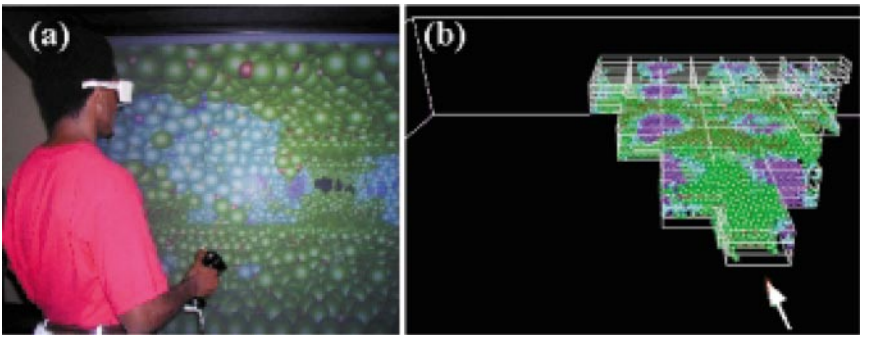

Figure 6 (*a*) A viewer immersed in and interacting with a MD simulation of a fractured ceramic nanocomposite (silicon nitride matrix reinforced with silica-coated silicon carbide fibers) rendered on a visualization platform called ImmersaDesk. The rendering involves an octree data structure for visibility culling. (*b*) Octree cells (bounded by *white lines*) dynamically approximate the current visible region (the position and viewing direction of the viewer is represented by the *white arrow*). Only the visible atoms are processed for rendering.

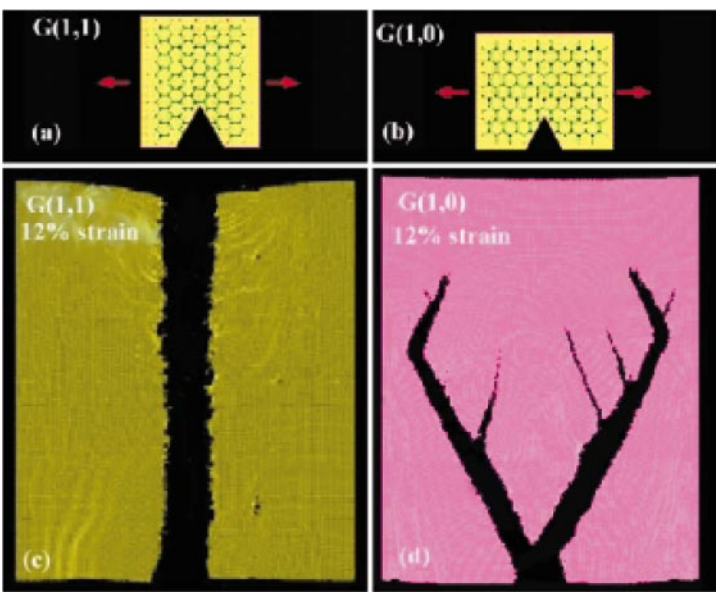

Figure 8 Orientations of a sheet of graphite (or graphine) for fracture simulations: (*a*) In the G(1,1) orientation, the applied strain is parallel to some of the C–C bonds; (*b*) in the G(1,0) orientation, the strain is perpendicular to some of the bonds. The *arrows* indicate the direction of the applied strain. Panels (*c*) and (*d*) display snapshots of fracture profiles of graphine at 12% of strain: (*c*) the G(1,1) orientation displays cleavage fracture; (*d*) multiple branching is observed in the G(1,0) orientation.

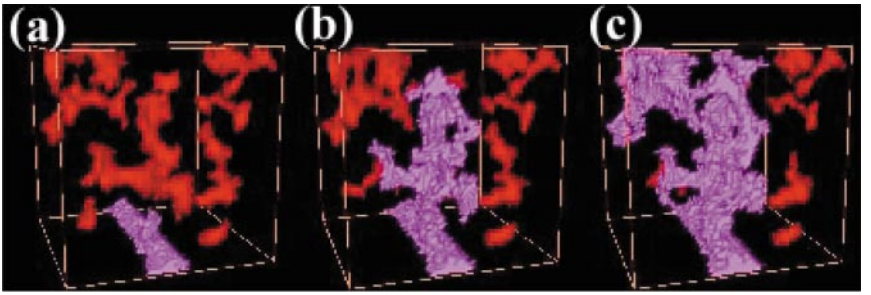

Figure 11 Snapshots showing evolution of cracks and pores in nanophase Si_3N_4 as the applied strain is increased. The crack front is shown in *purple* and isolated pores in *red* (dimension >6.4 nm^3). (*a*) Under an applied strain of 5%, small local branches appear near the notch. (*b*) As the strain is increased to 11%, the primary crack advances significantly by merging with pores. (*c*) When the strain reaches 14%, there is further coalescence of primary crack with pores.

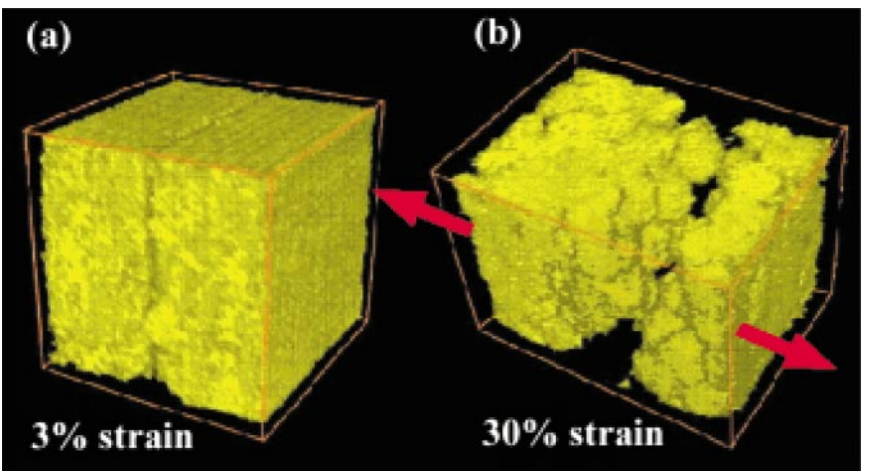

Figure 12 (*a*) Complete cleavage fracture in crystalline silicon nitride occurs at 3% of strain. (*b*) Fracture in nanophase silicon nitride at 30% of strain.

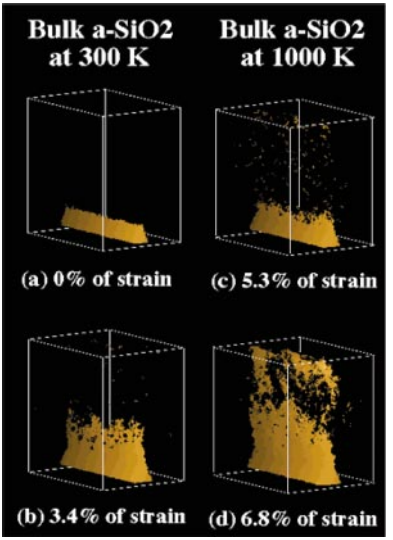

Figure 13 Snapshots of pores and cracks in bulk a-SiO_2 at 300 K (*a*) and (*b*) and at 1000 K (*c*) and (*d*); (*a*) shows the initial notch and (*b*) shows the evolution of several branches and nanoscale pores at a strain of 3.4%. (*c*) The system at 1000 K shows little progression of the pre-notch even at a strain of 5.3%. (*d*) Further increase in strain of 1.5% causes the crack front to move significantly and nanoscale pores to coalesce.

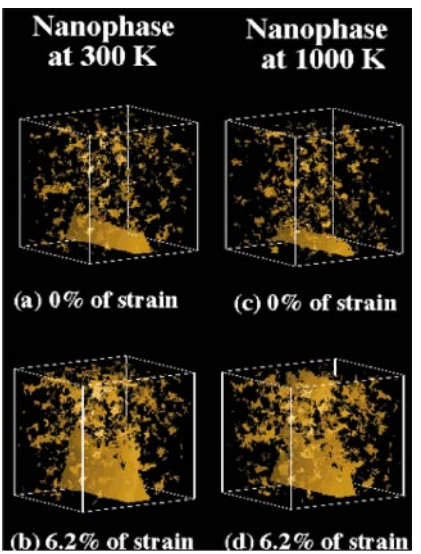

Figure 14 Snapshots of pores and cracks in nanophase SiO_2 at 300 K (*a*) and (*b*) and at 1000 K (*c*) and (*d*). In (*a*) and (*c*) the pores are in the interfacial regions between nanoparticles; (*b*) and (*d*) show the growth of pores and the evolution of the crack through the interfacial regions.

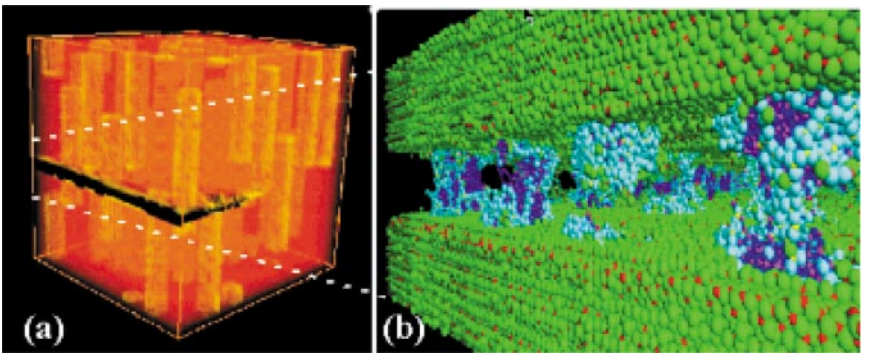

Figure 15 (*a*) Fracture in a nanocomposite consisting of silica-coated silicon carbide fibers (*yellow*) in a silicon nitride matrix (*red*). (*b*) Atomic view of fracture in the nanocomposite. The frictional fiber pull out enhances the toughness of the nanocomposite. Si atoms (*small red spheres*), N atoms (*large green spheres*), C atoms (*magenta*), and O atoms (*cyan*).

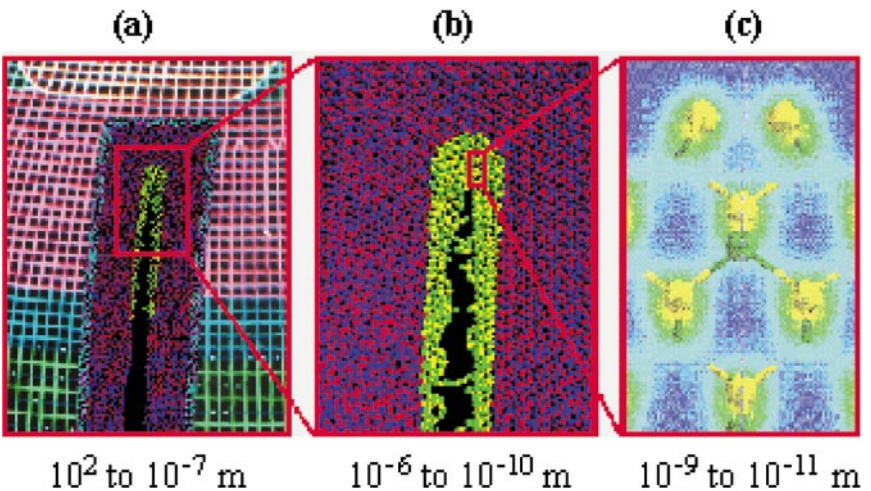

Figure 20 (*a*) Illustration of a hybrid finite-element (FE), molecular dynamics (MD), and quantum mechanical (QM) simulation of fracture. (*b*) The non-linear region near the crack is handled with the MD method. (*c*) A QM approach handles the crack-tip region in which bonds break or reform. Typical length scales covered by the FE, MD, and QM method are also shown.

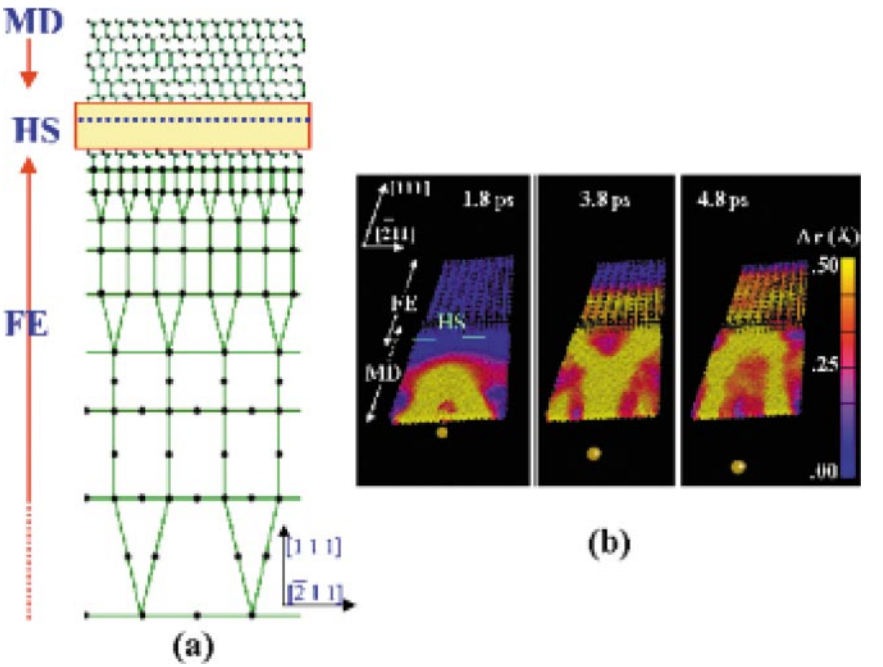

Figure 21 (*a*) Illustration of a hybrid FE/MD scheme for a three-dimensional silicon crystal for the crystallographic orientations (011). On the top is the MD region, where *spheres* and *lines* represent atoms and atomic bonds, respectively. At the bottom is the FE region, where *spheres* represent FE nodes, and FE cells are bounded by lines. Region enclosed between the *red lines* is the handshake (HS) region, in which particles are hybrid nodes/atoms; the *blue dotted line* within the HS region indicates the FE/MD interface. (*b*) Time evolution of FE nodes and MD atoms in a hybrid FE/MD simulation of a projectile impact on a silicon crystal. (The figure shows a thin slice of the crystal for clarity.) Absolute displacement of each particle from its equilibrium position is color-coded. No reflection is seen at the boundary.

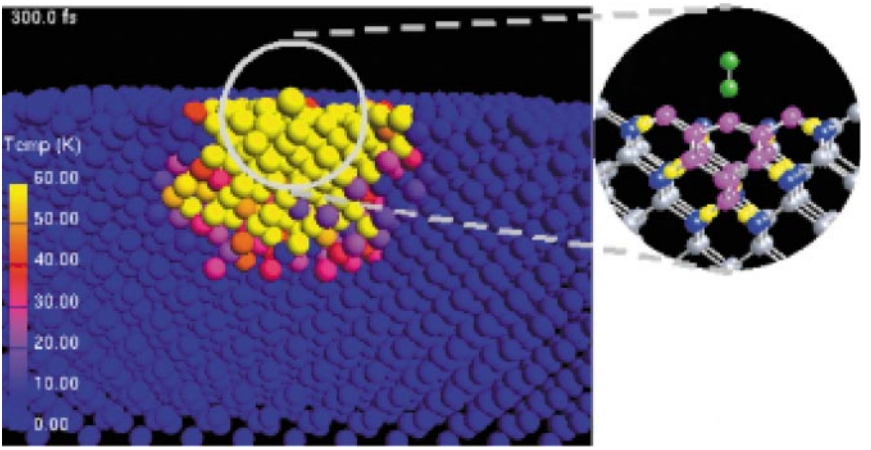

Figure 22 (*Right*) Initial configuration in the hybrid MD/DFT simulation for oxidation of Si (100) surface. *Magenta spheres* represent a cluster of silicon atoms; *gray*, the environment silicon atoms; *yellow*, hydrogen termination atoms for DFT calculations; *blue*, termination silicon atoms for MD calculations; and *green*, cluster oxygen atoms. (*Left*) Snapshot at 300 fs of a hybrid MD/DFT simulation of oxidation of a Si (100) surface. Colors represent kinetic energies of atoms in Kelvin.

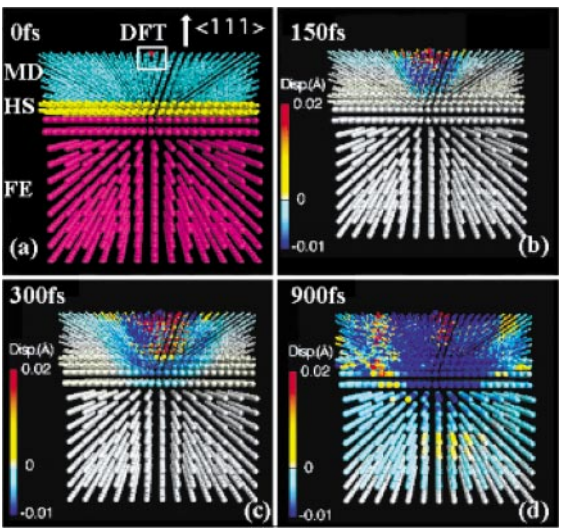

Figure 23 (*a*) An initial configuration of FE/MD/DFT simulation for oxidation of Si(100) surface. The *red* in the *small white box* shows the cluster of atoms treated by DFT, the *light blue* represents the MD region, the *magenta* represents the FE domain, and the *yellow* is the handshake between MD and FE. (*b–d*) Snapshots of the simulation where colors represent atomic displacements from the equilibrium positions. No reflection of displacement waves at the boundaries between FE and MD or between MD and DFT is observed.

Annual Review of Materials Research
Volume 32, 2002

CONTENTS

COMPUTATIONAL MATERIALS RESEARCH